High solar desalination efficiency achieved with three-dimensional Cu_2ZnSnS_4 nanosheet-assembled membranes

Chunhong Mu,[1] Yuanqiang Song,[1] Kai Deng,[1] Shuai Lin,[1] Yutie Bi,[2] Fabrizio Scarpa,[3] David Crouse[4]*

Prof. Y. Q. Song, Dr. C. H. Mu, K. Deng, S. Lin
School of Energy Science and Engineering, University of Electronic Science and Technology of China, 610054, People's Republic of China
E-mail: yuanqiangsong@uestc.edu.cn
Dr. Y. T. Bi
Fundamental Science on Nuclear Wastes and Environmental Safety Laboratory, Southwest University of Science and Technology, 621010, People's Republic of China
Prof. F. Scarpa
Bristol Centre for Nanoscience and Quantum Information, University of Bristol, BS8 1TR, United Kingdom
Prof. D. Crouse
Department of Electrical and Computer Engineering, Clarkson University, NY 13699, United States of America

Keywords: Cu_2ZnSnS_4 nanosheet, self-assemble, plasmon resonance absorption, solar desalination

ABSTRACT.
Plasmonic structures are gaining increasing tremendous interest due to its unique capability to trap light into subwavelength units, beneficial for high efficient light harvesting[1] and related applications. Here we present a plasmonic structures realized on a monocrystallized Cu_2ZnSnS_4 (CZTS) nanosheet-assembled membranes. This unique CZTS structure exhibits high absorption efficiency (~92.25%) in a broad solar spectrum (200-2500 nm), leading to a solar desalination efficiency of ~84.5% under 1 Sun irradiation. This highly efficient broadband absorption is due to the structure induced localized surface plasmon resonance (LSPR) absorption. Besides, owing to its high chemical stability, salty water containing heavy metal ions can be effectively desalinated with a constant long time (>20 hours) durability using this CZTS membranes as the absorber. The combination of the robust desalination effect, high stability and durability, as well as the low-cost and scalable process for production, make this type of CZTS membranes one of the most competitive desalination candidates.

To solve the increasingly severe water scarcity and pollution problem, a variety of technologies thus far have been developed.[2] Solar desalination technologies[3] are becoming much more popular due to its sustainable development with minimum environmental impacts. To achieve efficient solar desalination, as much of the incident solar energy as possible should be absorbed and converted into heat for use in the distillation process.

Plasmonic structures are gaining increasing tremendous interest due to its unique capability to trap light into subwavelength units, beneficial for high efficient light harvesting[1] It has been found that, metallic nanostructures with subwavelength unit size can hold LSPR heating effect,[4] leading to highly efficient light-to-heat conversion.[5] However in these

structures, noble metal materials are always used, and often photolithography, deposition under vacuum condition[1d),6] and nanostructured templates.[1a),5c)] These factors lead to higher costs for large-scale production and commercialization. So it becomes urgent to realize surface plasmon resonance (SPR) in conventional materials in order to obtain highly efficient solar energy harvest. There are three critical prerequisites required to realize SPR for maximum solar thermal utilization: (i) materials with high density of free charge carriers should be selected to obtain plasmonic properties;[6] (ii) materials should be fabricated into artificial assemblies of structured elements in subwavelength size.[7] In that way, the structured elements can excite surface plasmon polaritons with highly enhanced braodband absorption.[8] And also, the broadband absorption can be tunned by engineering the size and geometry of the structured elements.[9] (iii) besides, low-bandgap is demanded to match with solar spectra if semiconductors or metal oxides are adopted.

Bearing these requirements in mind, efficienct broadband absorption can most likely be realized in a class of heavily-doped, low-bandgap semiconductors, as long as it can be processed into suitable subwavelength size. In fact, there already exist a series of reports utilizing heavily-doped semiconductors to form good broadband absorbers by etching into specific micro-/nano-structures.[10] Cu_2ZnSnS_4 (CZTS) compound is a well-known non-toxic low-bandgap semiconductor widely used for solar cell applications.[11] It is a p-type seiconductor with a suitable direct energy bandgap, and a very high optical absorption coefficient (higher than 10^4 cm^{-1}).[12] Furthermore, CZTS are always found to have intrinsic high-density of free carriers with Cu-poor and Zn-rich elemental stoichiometry.[13] For the purpose of maximizing solar energy harvesting, it is desirable to widen the absorption spectra of CZTS. It has been reported that, Au NPs that embedded into CZTS can lead to a moderate broadened band absorption, which leads to a 100% increase of the power conversion efficiency of a photoelectrochemical solar cell.[14] There are other intensive studies, on noble metallic NPs enhanced absorbance in semiconductors, mainly focusing on improving their photocatalytic properties.[15] For further improvement of the broadband absorption, micro-structured CZTS membranes composed of elements in subwavelength size is quite necessary. In that case, SPR can be hold on the structure thus leading to a highly broadened absorption. However, fabrication of micro-/nano- patterned CZTS membranes are rarely reported especially aiming for its photothermal application.[16]

Here in this report, microporous CZTS membranes with typical plasmonic nanostructures (**Figure 2**) were successfully fabricated. The structures are assembled by ultrathin (~6 nm) monocrystallized CZTS nanosheets with varying submicron spatial gaps (0.1-0.6 μm). Such a size distribution of these spatial gaps just falls into the subwavelength range that can induce broadband LSPR absorption in solar spectrum,[17] thus producing a high optical absorption (~92.25%) through 200-2500 nm, which is comparable with that obtained from graphene oxide-based super absorbers.[7,18] Using this type of CZTS as the absorber, a high water evaporation rate of ~1.46 kg m^{-2} h^{-1} under 1 Sun irradiation can be obtained with long-time durability, reaching to a solar desalination efficiency of ~84.5%. Besides, salty water containing heavy metal ions can also be desalinated by this porous CZTS absorber due to its high chemical stability. Furthermore, the SPR effect found in the p-type CZTS semiconductor membranes with such a unique nanostructure makes it very promising for many other applications, such as photocatalysis[15i),19] and photovoltaics.[20]

The nanosheet-assembled CZTS membranes were synthesized *via* a facile process that includes ball milling and electrophoretic deposition (EPD), instead of using lithography or any templates. As shown in **Figure 1**(a), there are three main steps included in the synthetic process. Firstly, ultrafine CZTS NPs are synthesized *via* mechanical alloying by ball milling.

Secondly, EPD process is carried out using the CZTS NPs suspension as the electrophoretic solution, to obtain the precursor membranes. At last, high-temperature sintering is carried out to get the final nanostructures. From the X-ray diffraction (XRD) data shown in **Figure S1**, CZTS with the kesterite phase is formed in the first step *via* mechanical alloying process. The grain size in the formed CZTS ultrafine powders are typically distributed within the narrow range of 10-20 nm (**Figure S2**). The obtained CZTS NPs are then dispersed in solvents forming a uniform suspension ready for the subsequent EPD process. Additional details of the suspension solution are as follows. The solution includes a mixture of isopropanol, iodine, and ammonia that provides positive charges by forming $CH_3COCH_2I{\cdot}NH_4^+$ ligands,[21] as indicated in Figure 1(b). The absorbed $CH_3COCH_2I{\cdot}NH_4^+$ ligands on the CZTS NPs lead to a well-separated deposition of CZTS NPs on the cathode's surface, forming vertical standing CZTS thin stacks (Figure 1(b)) that themselves compose the precursor membranes. In the last step, high-temperature sintering will cause the removing of the absorbed ligands and the recrystallization of the CZTS NPs, leading to the final nanosheet-assembled microporous CZTS membranes. More detailed description of the growth mechanism is provided in **section I** in the supporting information.

Figure 2 provides the characterization of the nanosheet-assembled CZTS membranes. As shown in Figure 2(a), surface of the EPD-deposited CZTS precursor membranes is rough with many submicron-sized interstitials in it. The morphology is extraordinary changed after high-temperature sintering at 500 °C (CZTS-500), as shown in Figure 2(b) and (c). Clearly can be seen that, the final CZTS membranes are composed of ultrathin nanosheets, which are assembled into a honeycomb-like structure with varying submicron spatial gaps of 0.1-0.6 μm (Figure 2(b) and (c)). It should be emphasized that either lower or higher sintering temperature will deteriorate such an optimized nanostructure as observed in CZTS-500. As can be seen from **Figure S3**, CZTS membranes vulcanized at 450 °C (CZTS-450) have much thicker CZTS sheets with lower crystalline quality (**Figure S4**), while CZTS obtained at higher temperature (e.g. 550 °C, or CZTS-550 as shown in Figure S3) is totally transformed into particle films composed of large grains. Only the size distribution of spatial gaps that falls into the subwavelength range as observed in CZTS-500, can induce broadband LSPR absorption in solar spectrum.[17] For CZTS-500, the XRD (Figure S4), and high-resolution transmission electron microscopy (HRTEM) (Figure 2(c) and (d)) confirm the phase formation of kesterite CZTS (JCPDS 26-0575). The composed ultrathin CZTS nanosheets are monocrystallized (Figure 2(d) and the inset) with a typical thickness of ~6 nm (as confirmed by the HRTEM shown in the right-top inset of Figure 2(c)). The ultrathin thickness of the CZTS sidewall makes large portion of the comb unit cell be occupied by submicron holes, which could produce multipole surface plasmon polaritons at both sides of the CZTS nanosheet,[22] leading to a broadband optical absorption. It is obvious that the obtained CZTS membranes are black (Figure 2(f)), directly indicating of its efficient and broadband optical absorption. Such a unique nanostructure assembled by monocrystallized CZTS nanosheets could induce a broadband optical absorption through several mechanisms: (1) the presence of almost vertically-aligned CZTS nanosheets with an ultrathin thickness could reduce the reflective cross-section; (2) the size distribution (0.1-0.6 μm) of the spatial gaps between the adjacent CZTS nanosheets just falls into the subwavelength range that can induce a surface plasmon effect,[6,23] which will cause high-density LSPR effect and thus a broadband absorption through solar spectrum; (3) light trapping effect can be caused by the unique microporous features that will increase the internal light scattering[24] and thus enhance the absorption;[25] (4) abundant dangling bonds existing on the edges of the composed CZTS

nanosheets will also cause excessive density of states in CZTS's bandgap, which will lead to extra optical absorption beyond its intrinsic absorption limit.

To carefully examine these mechanisms, a three-dimensional (3D) finite difference time domain simulation has been employed, to evaluate the optical absorbance of the CZTS nanosheet-assembled microstructures, in which the variation of the unit size of the spatial gaps (d_{CZTS}) are considered (see **section II** of supporting information). As can be seen from **Figure 3**(a) that, with the decrease of d_{CZTS} from 1500 nm to 50 nm, the overall absorption increases with a distinct redshift. This implies stronger hybridization of neighboring surface plasmon occurs with the size decrease of the spatial gap between adjacent CZTS nanosheets.[1a)] Strong surface plasmonic hybridization will cause localized optical excitation and enhanced light focusing effect.[26] As can be seen from the simulated electric field distribution of the structures (e.g., d_{CZTS} = 100 nm as shown in Figure 3(b)), most of the incident energy is focused and trapped in the CZTS submicro-comb *via* LSPR effect.[27] Such a strong plasmonic hybridization and light trapping effect will cause efficient broadband absorption.

As can be seen from Figure 3(c), CZTS-500 membranes exhibit an ultra-high absorption efficiency (~92.25% on average) throughout the wavelength range of 200 nm to 2500 nm. In detail, the absorption declines from 300 nm to ~930 nm, but gains a re-increase trend after 930 nm (the pink color filled area in Figure 3(c)), which is distinctively different from that of CZTS thin films.[28] This absorption enhancement is diminished in CZTS-450 and even disappeared in CZTS-550 (Figure 3(c)). Such an enhanced absorption in the longer wavelength range observed in CZTS-500 can be attributed to LSPR absorption effect. The carrier (hole) concentration of the CZTS membranes obtained by Hall effect measurement is ~5×10^{18} cm^{-3}. Such a high carrier density as well as the unique nanostructure mentioned above provide two prerequisites to producing SPR effect.[6,8] More evidence for the occurrence of SPR is confirmed by Raman enhancement observed in this nanostructured CZTS membranes. As shown in Figure 3(d), the intensity of the main Raman peak from CZTS-500 increase significantly comparing with both of that from CZTS-450 composed of thicker CZTS sheets (Figure S3(a)), and that from CZTS-550 with large grain size (Figure S3(b)) (More detailed Raman deconvolution and explanation is in **section III** of supporting information and **Figure S5**). This Raman enhancement observed in CZTS-500 gives an evidence of the existence of SPR effect on CZTS surface, induced by the sharp edges of the assembled CZTS nanosheets.[29] With such a LSPR-enhanced efficient broadband absorption, the temperature on the CZTS membranes' surface can easily reach up to ~50 °C in ambient (25 °C with ~50% of humidity) under 1 Sun irradiation (**Figure S6**), meaning efficient photo-to-heat conversion. Efficient solar desalination can be expected on this CZTS membranes with such an excellent solar absorption.

Solar desalination experiments are realized *via* a simple duckweed imitation structure, as illustrated in **Figure 4**(a).[30] A polystyrene (PU) hard foam mold with low coefficient of thermal conductivity (~0.02 W/(m·K)) is attached underneath to let the CZTS-on-glass float on the water's surface. The foam mold also acts as an adiabatic layer to prevent heat loss. For the purpose of continuous water supply during evaporation, four small holes are drilled through the foam sidewalls (Figure 4(b)). By adjusting the mass of the foam, a thin water layer of 1-2 millimeters thick on the CZTS membranes' surface can be formed by the water infiltrating through the holes into the foam groove. Then the water on the CZTS membranes can be evaporated by the heat converted by the membranes' optical absorption. To evaluate the desalination efficiency, artificial seawater with the salinity of 3.5 wt% (Detailed ingredients are summarized in **Table S1**) is adopted for evaporation. Under 1 Sun irradiation,

the temperature of the water on CZTS surface can reach up to 44 °C (Figure 4(c)) in 3 minutes (**Figure S7**) without obvious temperature increase of the bulk water, which leads to a desalination rate of ~1.46 kg m^{-2} h^{-1}, and a corresponding solar steam efficiency reaches up to 84.5% (See detailed efficiency calculation in **section IV** and systematic discussion on steady-state energy balance in **Section V** of supporting information). The efficiency under 5 Sun irradiation is a little bit increased (~88.78%). Such an efficiency is comparable with recent solar desalination achievements as summarized in **Table S2**. Such an efficient liquid-to-vapor transition can be attributed to high photo-to-heat conversion efficiency, as well as the minimum heat loss from the desalination setup. Generally, higher evaporation efficiency can only be obtained by condensed higher solar power irradiation when using floating absorption layer for desalination,[1a),1b),31] while only medium efficiency (58%) can be obtained under 1 Sun irradiation[30] (See Table S2 of the desalination efficiency at varied irradiation). The high desalination efficiency (~84.5%) obtained under one Sun irradiation in our experiment is attributed to the following factors. (i) The SPR-induced high broadband absorption efficiency of such unique structured CZTS absorber is the main reason to the high light-to-heat conversion and thus the desalination efficiency. (ii) Vertically aligned CZTS nanosheets with sharp edges promote the release of vapor bubbles during desalination. When exposed to sun light, each CZTS nanosheet generates vapor bubbles from its top sharp edge. The lack of CZTS bulk and the ultra-small radius of curvature on the CZTS edge significantly accelerate the initial vapor nucleation and the overall steam generation dynamics.[32] (iii) Besides, the minimum heat loss during evaporation is another important contribution to the final high desalination efficiency. Firstly, thick polyurethane (PU) hard foam with low thermal conductivity (~0.02 W/(m·K)) is used as the absorber carrier, which thermally insulate the vicinity of the hot absorber from the liquid volume underneath, thus lead to the minimum heat loss. Furthermore, the initially produced micron scale vapor bubbles on CZTS nanosheets can reduce heat losses to the surrounding water medium due to the poor thermal conductivity of vapor, leading to a high steam generation rate.[33] In all, both the intrinsic structural factors and the set-up design contribute to the high solar desalination efficiency. Such a high desalination efficiency under low solar power irradiation will be very suitable for mini-type mobile desalination device. For example, it can conveniently provide fresh water for the man lost on a small wild island. More distinctively, our desalination setup demonstrates super long-time durability. During our desalination test, it works for 20 hours with a constant efficiency (Figure 4(c)) without any visible salts precipitation, exhibiting a robust long-time durability. In fact, the salt ions in the concentrated water above the CZTS membranes can timely diffuse out through the small holes on the foam sidewalls (Figure 4(b)). Such a long-time durability is significant for practical desalination application.

To further evaluate the desalination effect, the ions' concentrations in the distilled water were carefully tracked. As expected, concentrations of the four representative ions of Na^+, Ca^{2+}, Mg^{2+}, and K^+ are all strikingly decreased compared with that in the original solution, as shown in Figure 4(e). In fact, the ions concentration is lower than both the distilled water (1-50 mg/L) and membrane filtered water (10-500 mg/L).[34] Furthermore, due to the stability of CZTS compound, water containing heavy metal ions (Detailed ingredients are summarized in **Table S3)** can also be desalinated *via* our CZTS membranes absorber without visible surface corrosion. As shown in Figure 4(d), heavy metal ions of Cd^{2+}, Cu^{2+}, Cr^{3+}, and Pb^{2+} with concentration of 1 g/L can be reduced to 0.0027, 0.8336, 0.3331, and 0.1793 mg/L, respectively after desalination. This results demonstrate its robustness functionality in disposing chemical wastewater, which is very meaningful for chemical industry.

Cost-effectiveness of a solar desalination device is also important especially for commercialization. It should be noted that the CZTS-based absorber layer used in our device is not so cost-effective as reported just recently,[35] but the synthetic process of EPD used in our experiment is also scalable and productive, and the whole cost can be comparable to other achievements such as using AAO template supported, 3D printed graphene oxide textures, black gold membranes or graphene oxide layers as the absorber.[1a), 1b), 18] Furthermore, the sustainability and durability of our CZTS nanostructured absorber is not merely judged by its cost. As demonstrated in the desalination process, the synthesized CZTS absorber in our experiment is chemically inert, e.g., it can desalinate not only common salty water, but also water containing heavy metal ions, which makes it more suitable for purifying all types of industrial waste water. Besides, the long-time desalination without any visible salts precipitation, exhibiting its robust long-time durability. Therefore, though the CZTS absorber is not the most cost-effective candidate, its high chemical stability as well as the long-time durability compromise its relatively high-cost.

In all, 3D self-assembled CZTS membranes that are composed of monocrystallized nanosheets have been successfully fabricated, by using a convenient scalable route including ball milling and EPD procedures. The unique nanostructure of the synthesized CZTS membranes induces strong light focusing and LSPR heating effect, leading to an efficient broadband solar absorption (~92.25%) and an effective solar desalination (1.46 Kg m^{-2} h^{-1} under 1 Sun irradiation) with long-time durability. More importantly, our CZTS membranes can be used for desalination of water dissolving with both light and heavy metal ions, demonstrating its high durability and versatility. Besides, the SPR effect found in the CZTS membranes with such a unique nanostructure makes it very promising for many other applications, such as photocatalysis[15i),19] and photovoltaics.[20]

Experimental Section

Materials.

Ultrafine copper powder (Cu, >99.9%), zinc powder (Zn, >99.9%), and tin powder (Sn, >99.9%) were purchased from Beijing Dk nano S&T Ltd. The elemental sulfur powder (S), ethanol (CH_3CH_2OH), sodium borohydride ($NaBH_4$), ethylenediamine ($C_2H_8N_2$), polyethylene glycol (PEG, MW=8000), elemental iodine (I_2), isopropanol ($(CH_3)_2CHOH$), and ammonia (concentration of NH_3 is 20 wt%) in analytical purity were purchased from Chengdu Kelong chemical co. ltd. All commercial chemicals were used without further purification unless otherwise mentioned.

Synthesis of CZTS nanosheet-assembled membranes.

1) Synthesis of ultrafine CZTS precursor particles.

Under a dry Ar atmosphere, the mixture of Cu powder (1.9065 g, 0.03 mol), Zn (0.9809 g, 0.015 mol), Sn (1.7807 g, 0.015 mol), S (1.9240 g, 0.06 mol), CH_3CH_2OH (30 ml), and $C_2H_8N_2$ (6 ml), together with 30 g agate ball was introduced into a 70 ml nylon jar. The mixture was then milled for 48 hours using a home-made milling machine. After washing and centrifuging for three times a black precipitation was obtained from the mixed slurry. A black ultrafine powder (BUP) was then obtained from the precipitation after drying in a vacuum oven at 100 ^oC for 8 hours.

2) Synthesis of the CZTS nanosheet-assembled membranes *via* EPD process.

Dispersion A was obtained by mixing of 0.2 g BUP, 3 g PEG and 30 ml $(CH_3)_2CHOH$, *via* ultrasonic dispersion (30 minutes) followed by vigorous stirring for 1 hour. Dispersion B was produced by mixing of 5 g elemental I_2, 10 ml $(CH_3)_2CHOH$ and 20 ml AMMONIA *via* ultrasonic dispersion for 30 minutes. The dispersions A and B were mixed together in a

beaker *via* ultrasonic dispersion for 30 minutes followed by vigorous stirring to obtain a homogenous dispersion (named C). During the EPD process, Fluorine doped tin oxide (FTO) glass substrate was connected to cathode, and graphite as the opposite electrode. The optimized EPD process was carried out under 18 V for 15 minutes with the distance of 25 mm between two electrodes. The resulting samples on the FTO glass were then vulcanized at 450 ^{o}C, 500 ^{o}C and 550 ^{o}C for 30 minutes respectively, using N_2 as the inert gas and elemental sulfur as the active source.

Characterization.

XRD patterns were collected on a Bruker DX-1000 diffractometer with Cu Kα radiation (λ = 1.5406 Å). Field-emission scanning electron microscopy (FE-SEM) was carried out on a Hitachi S-4800. Transmission electron microscopy (TEM) was carried out using a CarlZeiss SMT PteLtd. Libra 200 FE. HRTEM, was performed using a JEOL JEM-ARF200F. Raman spectra measurements were performed on a Renishaw Raman spectroscope using a 325 nm line for the excitation. The power density was kept under 5 mW, which is low enough to avoid heating effects on samples. The optical absorption properties were identified in the wavelength range between 200 nm-2500 nm using a UV-vis spectrometer (UV3600, SHIMADZU), in which an integration sphere was used to collect the angles of the scattered light. The electrical properties are obtained by Hall effect measurement (tested on SWIN-Hall8800, Worldwide Co. Ltd) using the Van der Pauw method on a 5 mm × 5mm sample at room temperature. The Ohmic electrodes are made from Au. Ions concentration after desalination were traced using inductively coupled plasma emission spectrometer (Thermo iCAP6500, Thermo Fisher Ltd.).

Solar steam generation experiment.

During solar desalination test, standard solar simulators of Newport 94082A and Zolix - Sirus300P (Peking Zolix Instrument Ltd.) were adopted for 1 Sun and 5 Sun irradiation, respectively. Infrared thermal imager (FLIR E60 Infrared Camera, FLIR Systems Inc.) was used to capture the surface temperature during desalination. The set-up as illustrated in Figure 4a was adopted for collection of distilled water. The mass change of water during evaporation is obtained *via* another simple set-up. PU frame embedded with CZTS absorber is put into a large beaker containing enough water. The mass of the set-up is measured *via* a precise electronic scale. The mass reduction of the whole beaker during evaporation equals to the mass of evaporated water.

Supporting Information

Supporting Information is available from the Wiley Online Library or from the author.

Acknowledgements

This work is financially supported by the National Natural Science Foundation of China grant no. 51402042, Science and Technology Support Program of Sichuan Provincial Science and Technology Department (no. 2016GZ0248), School project of UESTC (no. A03013023001041), and the Fundamental Science on Nuclear Wastes and Environmental Safety Laboratory (no. 14zxnk04).

Received: ((will be filled in by the editorial staff))
Revised: ((will be filled in by the editorial staff))
Published online: ((will be filled in by the editorial staff))

References

[1] a) L. Zhou, Y. Tan, J. Wang, W. Xu, Y. Yuan, W. Cai, S. Zhu, J. Zhu, *Nat. Photon.* **2016**, *10*, 393; b) L. Zhou, Y. Tan, D. Ji, B. Zhu, P. Zhang, J. Xu, Q. Gan, Z. Yu, J. Zhu, *Sci. Adv.* **2016**, *2*, e1501227; c) H. A. Atwater, A. Polman, *Nat. Mater.* **2010**, *9*, 205; d) K. Aydin, V. E. Ferry, R. M. Briggs, H. A. Atwater, *Nat. Commun.* **2011**, *2*, 517.
[2] a) M. Elimelech, W. A. Phillip, *Science* **2011**, *333*, 712; b) G. Xiao, X. Wang, M. Ni, F. Wang, W. Zhu, Z. Luo, K. Cen, *Appl. Energ.* **2013**, *103*, 642.
[3] H. Sharon, K. S. Reddy, *Renew. Sust. Energ. Rev.* **2015**, *41*, 1080.
[4] K. A. Willets, R. P. V. Duyne, *Annu. Rev. Phys. Chem.* **2007**, *58*, 267.
[5] a) Z. Fang, Y.-R. Zhen, O. Neumann, A. Polman, F. J. García de Abajo, P. Nordlander, N. J. Halas, *Nano Lett.* **2013**, *13*, 1736; b) Y. Xiong, R. Long, D. Liu, X. Zhong, C. Wang, Z.-Y. Li, Y. Xie, *Nanoscale* **2012**, *4*, 4416; c) K. Bae, G. Kang, S. K. Cho, W. Park, K. Kim, W. J. Padilla, *Nat. Commun.* **2015**, *6*, 10103; d) G. Tagliabue, H. Eghlidi, D. Poulikakos, *Sci. Rep.* **2014**, *4*, 7181.
[6] J. M. Luther, P. K. Jain, T. Ewers, A. P. Alivisatos, *Nat. Mater.* **2011**, *10*, 361.
[7] a) X. Li, W. Xu, M. Tang, L. Zhou, B. Zhu, S. Zhu, J. Zhu, *Proc. Natl. Acad. Sci. U.S.A.* **2016**, *113*, 13953; b) X. Hu, W. Xu, L. Zhou, Y. Tan, Y. Wang, S. Zhu, J. Zhu, *Adv. Mater.*, DOI: 10.1002/adma.201604031.
[8] D. R. Smith, J. B. Pendry, M. C. K. Wiltshire, *Science* **2004**, *305*, 788.
[9] C. M. Watts, X. Liu, W. J. Padilla, *Adv. Mater.* **2012**, *24*, OP98.
[10] a) K.-Q. Peng, S.-T. Lee, *Adv. Mater.* **2011**, *23*, 198; b) Y.-F. Huang, S. Chattopadhyay, Y.-J. Jen, C.-Y. Peng, T.-A. Liu, Y.-K. Hsu, C.-L. Pan, H.-C. Lo, C.-H. Hsu, Y.-H. Chang, C.-S. Lee, K.-H. Chen, L.-C. Chen, *Nat. Nano.* **2007**, *2*, 770; c) J. Zhu, Z. Yu, G. F. Burkhard, C.-M. Hsu, S. T. Connor, Y. Xu, Q. Wang, M. McGehee, S. Fan, Y. Cui, *Nano Lett.* **2009**, *9*, 279; d) Z. Fan, R. Kapadia, P. W. Leu, X. Zhang, Y.-L. Chueh, K. Takei, K. Yu, A. Jamshidi, A. A. Rathore, D. J. Ruebusch, M. Wu, A. Javey, *Nano Lett.* **2010**, *10*, 3823.
[11] a) S. Ahmed, K. B. Reuter, O. Gunawan, L. Guo, L. T. Romankiw, H. Deligianni, *Adv. Energy Mater.* **2012**, *2*, 253; b) W. Wang, M. T. Winkler, O. Gunawan, T. Gokmen, T. K. Todorov, Y. Zhu, D. B. Mitzi, *Adv. Energy Mater.* **2014**, *4*, 1301465; c) W. Huang, Q. Li, Y. Chen, Y. Xia, H. Huang, C. Dun, Y Li, D. L. Carroll, *Sol. Energ. Mat. Sol. C.* **2014**, *127*, 188.
[12] a) T. Tanaka, T. Nagatomo, D. Kawasaki, M. Nishio, Q. Guo, A. Wakahara, A. Yoshida, H. Ogawa, *J. Phys. Chem. Solids* **2005**, *66*, 1978; b) S. S. Mali, P. S. Shinde, C. A. Betty, P. N. Bhosale, Y. W. Oh, P. S. Patil, *J. Phys. Chem. Solids* **2012**, *73*, 735; c) S. S. Mali, B. M. Patil, C. A. Betty, P. N. Bhosale, Y. W. Oh, S. R. Jadkar, R. S. Devan, Y.-R. Ma, P. S. Patil, *Electrochim. Acta* **2012**, *66*, 216.
[13] a) A. Nagaoka, K. Yoshino, H. Taniguchi, T. Taniyama, H. Miyake, *J. Cryst. Growth* **2012**, *341*, 38; b) T. P. Dhakal, C. Y. Peng, R. Reid Tobias, R. Dasharathy, C. R. Westgate, *Sol. Energy* **2014**, *100*, 23; c) S. K. Swami, A. Kumar, V. Dutta, *Energy Procedia* **2013**, *33*, 198.
[14] X. Zhang, X. Wu, A. Centeno, M. P. Ryan, N. M. Alford, D. J. Riley, F. Xie, *Sci. Rep.* **2016**, *2*, 23364.
[15] a) B. Ding, B. J. Lee, M. Yang, H. S. Jung, J.-K. Lee, *Adv. Energy Mater.* **2011**, *1*, 415; b) J. Li, S. K. Cushing, J. Bright, F. Meng, T. R. Senty, P. Zheng, A. D. Bristow, N. Wu, *ACS Catal.* **2013**, *3*, 47; c) B. Wu, D. Liu, S. Mubeen, T. T. Chuong, M. Moskovits, G. D. Stucky, *J. Am. Chem. Soc.* **2016**, *138*, 1114; d) C.-H. Kuo, T.-E. Hua, M. H. Huang, *J. Am. Chem. Soc.* **2009**, *131*, 17871; e) L. Zhang, D. A. Blom, H. Wang, *Chem. Mater.* **2011**, *23*, 4587; f) A. Sousa-Castillo, M. Comesaña-Hermo, B. Rodríguez-González, M. Pérez-Lorenzo, Z. Wang, X.-T. Kong, A. O. Govorov, M. A. Correa-Duarte, *J. Phys. Chem. C* **2016**, *120*, 11690; g) B.-H. Wu, W.-T. Liu, T.-Y. Chen, T.-P. Perng, J.-H. Huang, L.-J. Chen, *Nano Energy* **2016**, *27*, 412; h) M. Wang, M. Ye, J. Iocozzia, C. Lin, Z. Lin, *Adv. Sci.* **2016**, *3*, 1600024; i) C. Clavero, *Nat. Photon.* **2014**, *8*, 95.

[16] a) E. Ha, L. Y. S. Lee, H.-W. Man,S. C. E. Tsang, K.-Y. Wong, *ACS Appl. Mater. Interfaces* **2015**, *7*, 9072; b) B.-J. Li, P.-F. Yin, Y.-Z. Zhou, Z.-M. Gao, T. Ling, X.-W. Du, *RSC Adv.* **2015**, *5*, 2543; c) W. Bi, M. Zhou, Z. Ma, H. Zhang,J. Yu, Y. Xie, *Chem. Commun.* **2012**, *48*, 9162.
[17] E. Petryayeva, U. Krull, J. *Anal. Chim. Acta* **2011**, *706*, 8.
[18] Y. Li, T. Gao, Z. Yang, C. Chen, W. Luo, J. Song, E. Hitz, C. Jia, Y. Zhou, B. Liu, B. Yang, L. Hu, *Adv. Mater.*, DOI: 10.1002/adma.201700981.
[19] a) X. Chen, S. Shen, L. Guo, S. S. Mao, *Chem. Rev.* **2010**, *110*, 6503; b) S. K. Cushing, J. Li, J. Bright, B. T. Yost, P. Zheng, A. D. Bristow, N. Wu, *J. Phys. Chem. C* **2015**, *119*, 16239.
[20] S. S. Mali, P. S. Patil, C. K. Hong, *ACS Appl. Mater. Interfaces* **2014**, *6*, 1688.
[21] L. Dusoulier,R. Cloots, B. Vertruyen, R. Moreno, O. Burgos-Montes, B. Ferrari, *J. Eur. Ceram. Soc.* **2011**, *31*, 1075.
[22] M. Nishida, N. Hatakenaka, Y. Kadoya, *Phys. Rev. B* **2015**, *91*, 235406.
[23] a) D. Dorfs, T. Härtling, K. Miszta, N. C. Bigall, M. R. Kim, A. Genovese, A. Falqui, M. Povia, L. Manna, *J. Am. Chem. Soc.* **2011**, *133*, 11175; b) F. Scotognella, G. Della Valle, A. R. Srimath Kandada, M. Zavelani-Rossi, S. Longhi, G. Lanzani, F. Tassone, *Eur. Phys. J. B* **2013**, *86*, 1.
[24] J. Q. Xi, M. F. Schubert, J. K. Kim, E. F. Schubert, M. Chen, S.-Y. Lin, W. Liu, J. A. Smart, *Nat. Photon.* **2007**, *1*, 176.
[25] M.-F. Xu, X.-Z. Zhu, X.-B. Shi, J. Liang, Y. Jin, Z.-K. Wang, L.-S. Liao, *ACS Appl. Mater. Interfaces* **2013**, *5*, 2935.
[26] K. Li, M. I. Stockman, D. J. Bergman, *Phys. Rev. Lett.* **2003**, *91*, 227402.
[27] J. B. Chou, Y. X. Yeng, Y. E. Lee, A. Lenert, V. Rinnerbauer, I. Celanovic, M. Soljačić, N. X. Fang, E. N. Wang, S.-G. Kim, *Adv. Mater.* **2014**, *26*, 8041.
[28] a) N. M. Shinde, R. J. Deokate, C. D. Lokhande, *J. Anal. Appl. Pyrol.* **2013**, *100*, 12; b) J.-S. Seol, S.-Y. Lee, J.-C. Lee, H.-D. Nam, K.-H. Kim, *Sol. Energ. Mater. Sol. C.* **2003**, *75*, 155.
[29] a) C. G. Khoury, T. Vo-Dinh, *J. Phys. Chem. C* **2008**, *112*, 18849; b) E. Nalbant Esenturk, A. R. Hight Walker, *J. Raman Spectrosc.* **2009**, *40*, 86.
[30] L. Zhang, B. Tang, J. Wu, R. Li, P. Wang, *Adv. Mater.* **2015**, *27*, 4889.
[31] H. Ghasemi, G. Ni, A. M. Marconnet, J. Loomis, S. Yerci, N. Miljkovic, G. Chen, *Nat. Commun.* **2014**, *5*, 4449.
[32] M. S. Zielinski, J.-W. Choi, T. L. Grange, M. Modestino, S. M. H. Hashemi, Y. Pu, S. Birkhold, J. A. Hubbell, D. Psaltis, *Nano Lett.* **2016**, *16*, 2159.
[33] A. Polman, *ACS nano* **2013**, *7*, 15.
[34] a) Safe Drinking-Water from Desalination (WHO, 2011), http://www.who.int/water_sanitation_health/publications/desalination_guidance/en/, accessed: April, 2017; b) S. P. Surwade, S. N. Smirnov, I. V. Vlassiouk, R. R. Unocic, G. M. Veith, S. Dai, S. M. Mahurin, *Nat. Nano.* **2015**, *10*, 459.
[35] Z. Liu, H. Song, D. Ji, C. Li, A. Cheney, Y. Liu, N. Zhang, X. Zeng, B. Chen, J. Gao, Y. Li, X. Liu, D. Aga, S. Jiang, Z. Yu, Q. Gan *Global Challenges* **2017**, *1*, 1600003.

Figure 1. (a) Schematic illustration of the synthetic process, (b) and (c), the formation mechanism of the self-assembled CZTS nanosheets.

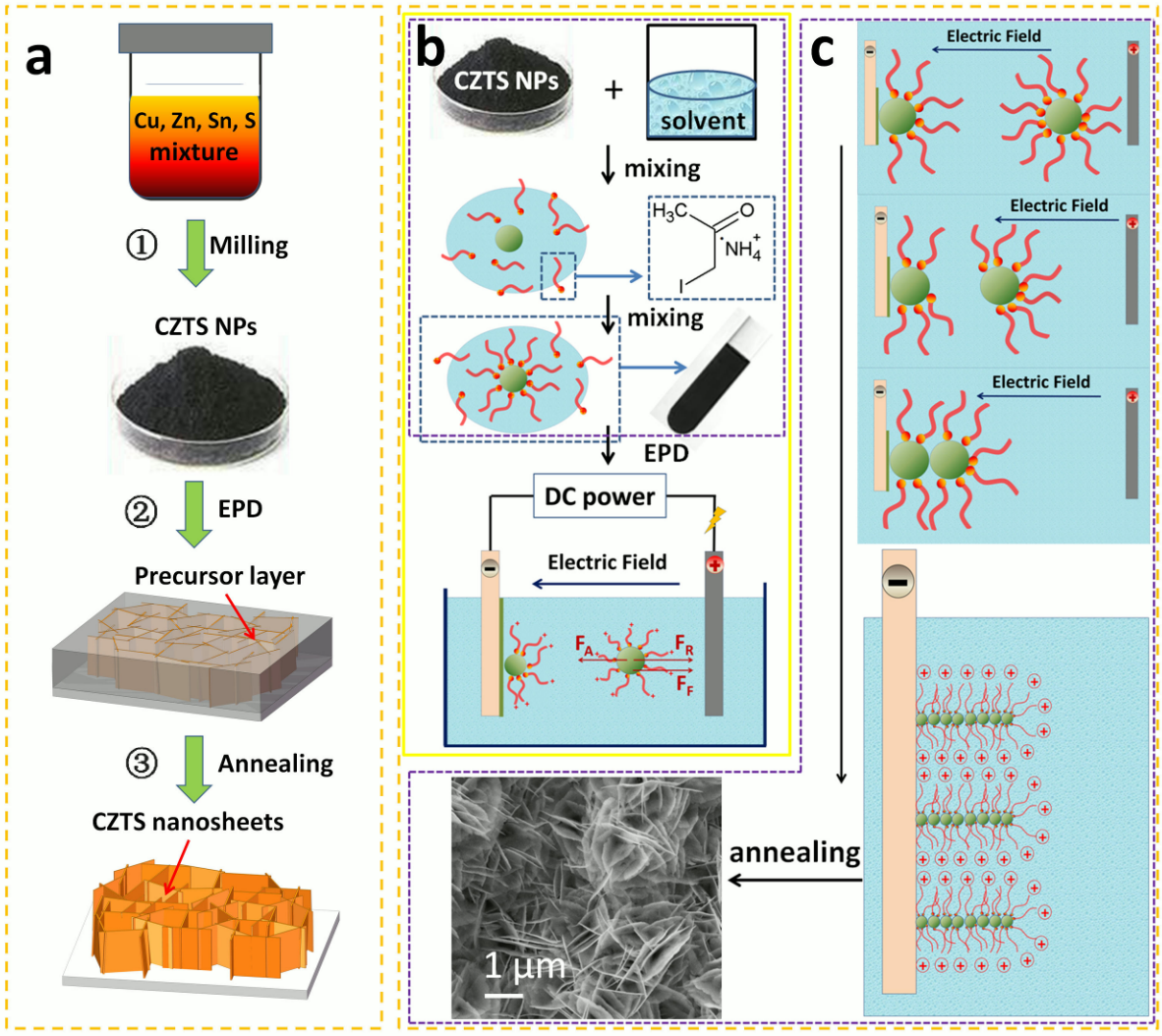

Figure 2. Characterization of the honeycomb-like CZTS microporous membranes. (a) SEM image of the EPD-deposited CZTS precursor layer obtained *via* EPD process. (b) and (c) are SEM images of the final CZTS membranes after high-temperature sintering. (d) and (e), are TEM images. The left-top inset in (d) of the selected area electron diffraction indicates the formation of the kesterite CZTS phase, while the right-top inset in (d) shows the thickness of one CZTS nanosheet. The inset in (e) clearly demonstrate the crystalline parameters corresponding to the kesterite CZTS phase. (e) an optical photograph of the fabricated CZTS membranes.

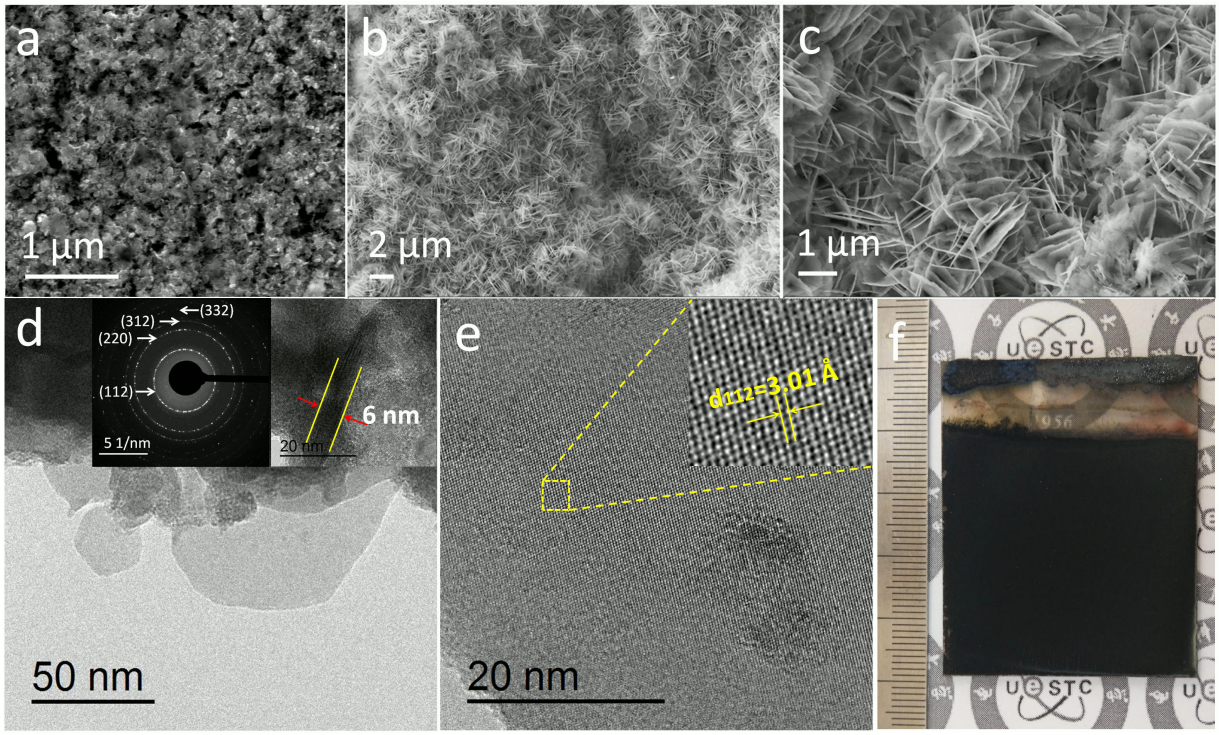

Figure 3. (a) the simulated absorption spectra of the CZTS nanosheet arrays with varied unit size length (d_{CZTS}) ranging from 50 nm to 1500 nm, and (b) the electric field distribution of the CZTS nanosheet arrays with d_{CZTS} = 100 nm. Both sectional view and top view of the electric field distribution are given for clarity purpose. In the images, the parts enclosed by the green dotted line represent CZTS. (c) the experimental optical absorption spectra of the CZTS membranes obtained by annealing at 450 ^{0}C (CZTS-450), 500 ^{0}C (CZTS-500), and 550 ^{0}C (CZTS-550), respectively. (d) Raman spectra of the different CZTS membranes.

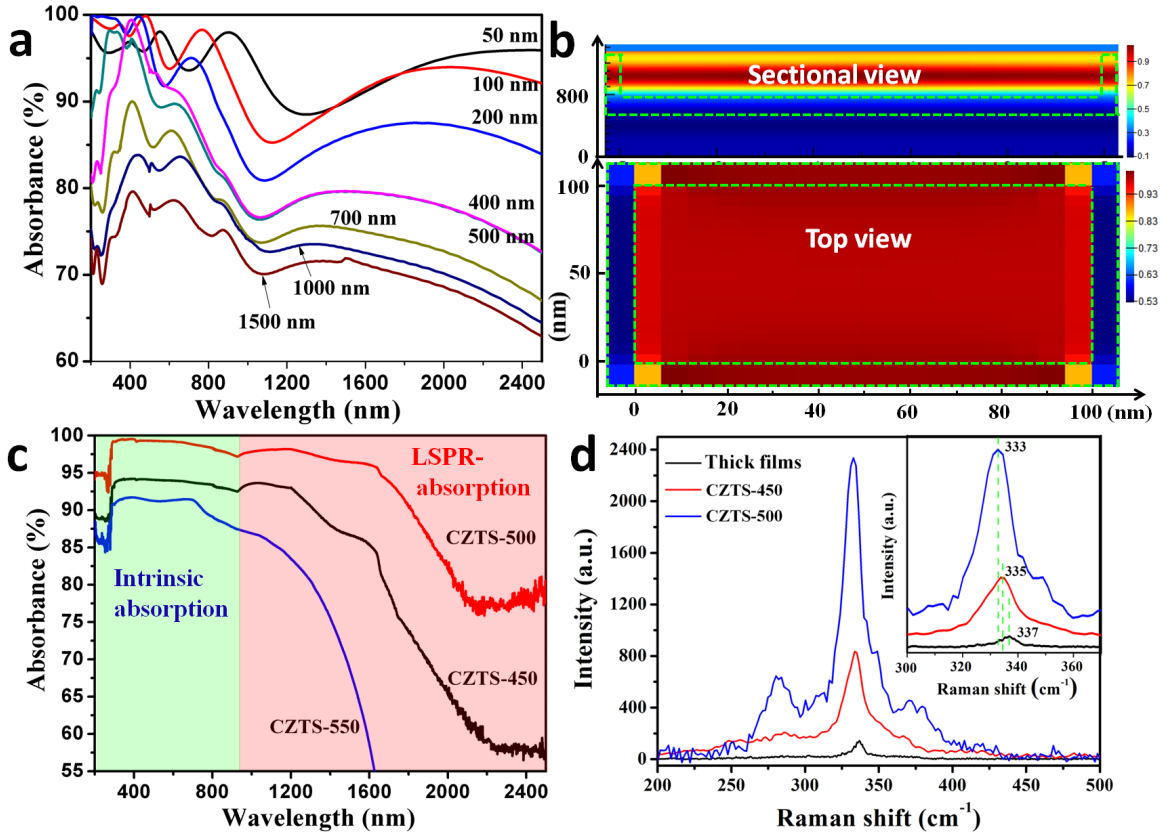

Figure 4. (a) schematic of the solar desalination experimental set-up, and (b) schematic illustration of the foam box design for evaporation. (c) evaporation rates with and without CZTS absorbers over time and under different optical concentrations of C_{opt}=1 and C_{opt}=5, respectively. CZTS (C_{opt}=0) indicates the evaporation rate using CZTS absorber without irradiation, which is adopted as the reference to be subtracted to calculate the precise evaporation efficiency. (d) the measured concentrations of ions before and after desalination, using an artificial seawater sample (with the salinity of 3.5 wt% as summarized in Table S1) and the water that containing heavy metal ions (the composition is summarized in Tables S3).

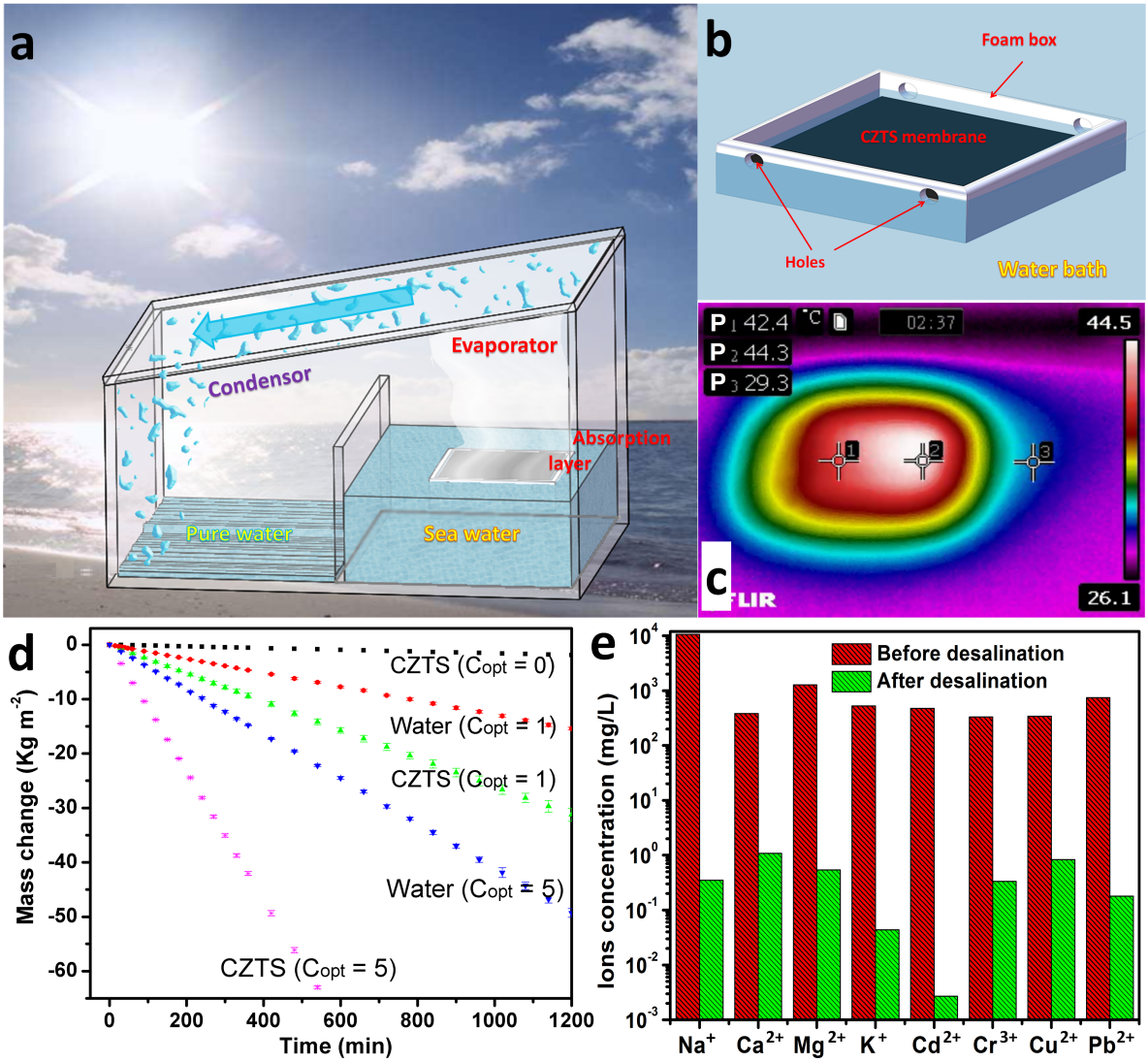

Plasmonic CZTS membranes assembled by ultrathin (~6 nm) monocrystallized nanosheets with varying submicron spatial gaps (0.1-0.6 μm) are synthesized. This unique structures induce surface-plasmon-resonance effect, leading to a high-broadband absorption (~92.25%) through 200-2500 nm, which in turn produces a high water evaporation rate of ~1.46 kg m^{-2} h^{-1} under 1 Sun irradiation with long-time durability.

Keyword Cu_2ZnSnS_4 nanosheet, self-assemble, plasmon resonance absorption, solar desalination

Chunhong Mu, Yuanqiang Song,* Kai Deng, Shuai Lin, Yutie Bi, Fabrizio Scarpar, David Crouse

High solar desalination efficiency achieved with three-dimensional Cu_2ZnSnS_4 nanosheet-assembled membranes

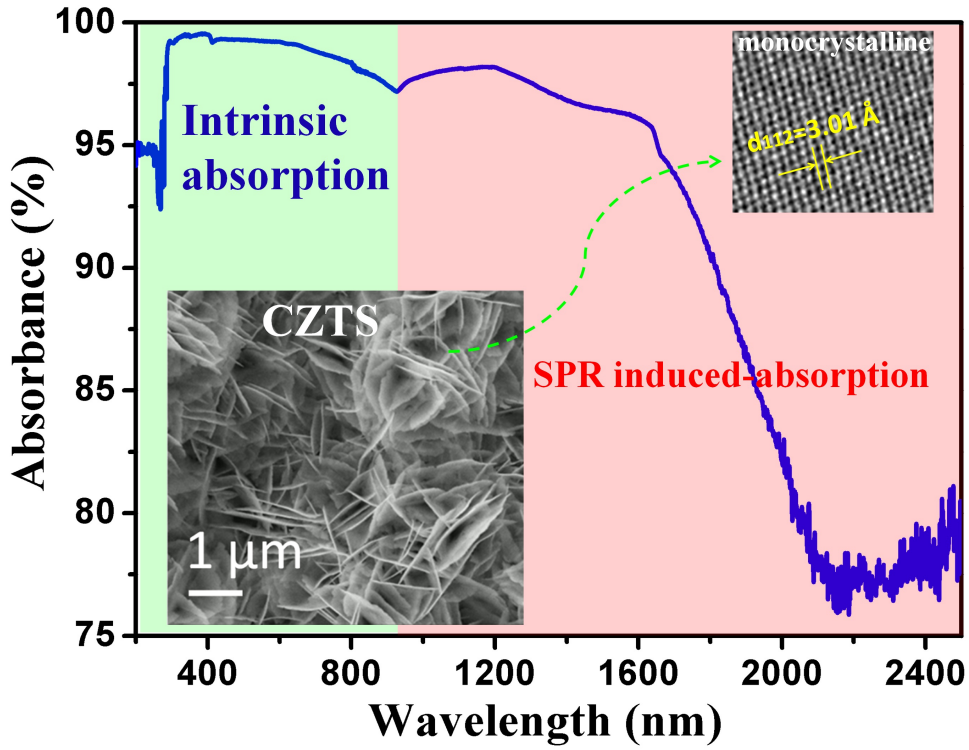

Supporting Information

High solar desalination efficiency achieved with three-dimensional Cu_2ZnSnS_4 nanosheet-assembled membranes

Chunhong Mu,[1] Yuanqiang Song,[1] Kai Deng,[1] Shuai Lin,[1] Yutie Bi,[2] Fabrizio Scarpar,[3] David Crouse[4]*

Section I. Formation mechanism of self-assembled CZTS nanosheets.

The following explanation for the formation mechanism of the nanosheet-assembled CZTS membranes *via* EPD process is based on Figure 1. The adopted suspension for EPD is prepared by mixing the previously obtained CZTS NPs with a certain amount of isopropanol, iodine, and ammonia. It is known that isopropanol can be converted into acetone *via* a reversible reaction described as: $(CH_3)_2CHOH + I_2 \rightleftharpoons (CH_3)_2CO + 2HI$. Acetone can be further converted into positively charged ligands of $CH_3CH_2ICOH^+$ *via* complex chemical reactions and equilibriums described as follow:[S1]

$(CH_3)_2CO + I_2 \rightleftharpoons (CH_3)_2CO^{+}\cdot I_2^{-}$

$(CH_3)_2CO + I_2 \longrightarrow CH_3COCH_2I + I^- + H^+ \longrightarrow CH_3COCH_2I\cdot H^+ + I^-$

In our experiment, with the addition of ammonia into the isopropanol-iodine solution, $CH_3COCH_2I\cdot H^+$ is supposed to evolve into $CH_3COCH_2I\cdot NH_4^+$ by absorbing one ammonia molecular:

$CH_3CH_2ICOH^+ + NH_3\cdot H_2O \rightleftharpoons CH_3COCH_2I\cdot NH_4^+ + H_2O$

As illustrated in Figure 1(b), $CH_3COCH_2I\cdot NH_4^+$ ligands are supposed to be absorbed on CZTS NPs' surface forming a positively charged CZTS NPs that can be uniformly dispersed and suspended in the solution. In EPD process, positively charged CZTS NPs will experience three forces as illustrated in Figure 1(b): the electrostatic attracting force (F_A) *via* electric field between two electrodes, the electrostatic repulsion force (F_R) originated from previously deposited positively charged NPs and the friction force (F_F) due to the continuous movement toward the cathode. Only when $F_A > (F_R + F_F)$ the EPD process can continue and the thickness of the deposited CZTS layers increase. When a CZTS NP approaches the previously deposited CZTS NPs, the ligands in the head-to-head area of two opposite NPs will be repulsed laterally by the friction F_R (Figure 1(c)). Under the conditions of $F_A > (F_R + F_F)$, the CZTS NP will be pushed forward and finally attached to the previously deposited CZTS NP. The assembling process will continue as long as $F_A > (F_R + F_F)$, but the CZTS NPs along the substrate plane will start to be separated apart due to steric effects and electrostatic repulsion caused by the absorbed positively charged ligands of the $CH_3COCH_2I\cdot NH_4^+$. Therefore, with the continuation of the EPD process the well-separated CZTS NPs assembled stacks will grow on the substrate.

This mechanism also explains why many interstitials appear in the EPD synthesized CZTS precursor membranes (Figure 2(a)). With the removal of the absorbed ligands by high-temperature annealing, the nanosheet-assembled microporous CZTS membranes can therefore be obtained.

Section II. Simulation methods and details. Absorption spectrum calculations of the 3D honeycomb-like CZTS membranes. Modelling was performed by the FDTD method (FDTD solutions V8.6, lumerical). To calculate the total absorption performance of the microporous CZTS absorber, a simplified FDTD-based optical modeling with one-side missed square-shaped CZTS box array on glass substrate is used to simulate the actual 3D plasmonic nanostructure. For the CZTS box, the thickness of the bottom side (*t*) is kept as 300nm, the thickness of the four sides (d) is kept as 6 nm, the height of the box is 500 nm, with the variation of the unit size of the CZTS box (d_{CZTS}) as 50 nm, 100 nm, 400 nm, 1000 nm, 1500 nm, respectively. The material parameter of CZTS is using the data from the ref. [S2]. During the simulation, the period boundary condition and the perfect match condition (PMC) are adopted in the *X*-*Y* direction, and *Z* direction, respectively.

Section III. Analysis of Raman spectra from different CZTS membranes.
It can be seen that, all Raman spectra show a main peak located at 333-337 cm^{-1}, which can be definitely attributed to CZTS with kesterite phase.[S3] Deconvolution peaks of CZTS-500 at 282 cm^{-1}, 333 cm^{-1}, and 375 cm^{-1} (Figure S5(a)), which can be all attributed to the CZTS, confirm its phase purity.[S3] It is noted that the intensity of the main peak increases significantly from 100 counts for CZTS-550 to 2400 counts for the EPD-synthesized CZTS-500 (Figure 3(d)). This Raman enhancement observed in the nanostructured CZTS-500 gives an evidence of the existance of SPR effect on CZTS surface, induced by the sharp edges of the assembled nanosheets.[S4] The SPR effect on CZTS surface may absorb photons with energy below the E_g value,[S5] leading to the final high absorption in a wide spectra range out of E_g limitation. There is also the presence of an obvious blue shift of the main peak from337 cm^{-1} to 333 cm^{-1}, with the morphology transformation from a thick film with large grains (Figure S3(b)) to a nanostructred microporous feature (Figure 2(b-c)). The blue shift is due to the highly decreased grain size in nanostructured CZTS.[S6]

Section IV. Calculation of the solar evaporation efficiency. The solar evaporation efficiency η can be calculated by the following formula[S7]

$$h_{LV}\eta = mh_{LV} / C_{opt}P_0 \qquad \text{[S1]}$$

in which m is the mass flux, h_{LV} is the latent enthalpy of the liquid-vapor phase change (the values of h_{LV} adopted in the calculation are the same with that in ref. [S7]). C_{opt} is the solar irradiation power of one sun (1 kW m^{-2}), and $C_{opt}P_0$ refers to the illumination intensity on the absorber surface. To get the precise solar evaporation efficiency, the evaporation rate without irradiation (CZTS (C_{opt} = 0) as indicated in Figure 4(d)) is measured and subtracted.
Section V. Calculation and discussion of the steady-state energy balance during solar evaporation. As illustrated in Figure S8, under a steady-state condition, the total heat losses (Q_T) during solar evaporation consists of: (i) heat conduction loss from the heated water to bulk water underneath through PU mold ($Q_{C\text{-}PU}$), and that through the four small holes on side ($Q_{C\text{-}Holes}$), (ii) heat conduction loss from the heated water to the air above ($Q_{C\text{-}Air}$), and

(iii) Radiation heat flux from the CZTS absorber ($Q_{R\text{-}CZTS}$). That is, Q_T= ($Q_{C\text{-}PU}$) + $Q_{C\text{-}Holes}$ + $Q_{C\text{-}Air}$ + $Q_{R\text{-}CZTS}$. The conduction loss was calculated based on the Fourier's law

$$q = -k\nabla T, \quad \text{[S2]}$$

where q denotes the heat, k is the thermal conductivity of material, and ∇T is temperature gradient, determined by the temperature difference between the hot zone and the cold zone, and the thickness of the diabetic layer between them. The thermal conductivity of PU hard foam is ~0.02 W/(m·K), the thickness of the PU wall adopted in the evaporation set-up is 1 cm. The temperature of the hot water and the bulk water is 44.3 ^{o}C and 25 ^{o}C, respectively. Thus based on Eq. **S2**, we can calculate that the conduction heat loss from PU wall ($Q_{C\text{-}PU}$) accounts for 3.86% of all irradiation energy. The minimum heat loss from PU wall is confirmed by the profile temperature distribution, as shown in Figure S7. As can be seen that, no obvious temperature increase for bulk water even after 1 hour solar evaporation. As the diameter of each hole is about 1 mm, the conduction heat loss from the four small holes can be omitted. It should be noted that, holes should be as small as possible, as long as it can provides enough water for steady solar evaporation. In our experiment, four holes on side with the diameter of ~1 mm can sustain the solar evaporation. But the heat loss of $Q_{C\text{-}Air}$ can hardly be calculated, as the thermal field distribution above the absorber is unknown. It can predict that there is a gradient temperature distribution in the thick hot air above the absorber, which will effectively block the heat loss. Besides, as the infrared emission coefficient of CZTS absorber is also unknown, the radiation loss can hardly be calculated either. In fact, even if CZTS produce certain infrared emission, it can be partially absorbed by the water layer above the CZTS absorber.

Figure S1. XRD of the CZTS precursors obtained by ball milling with different time durations. With increasing milling time from 12 hours to 36 hours, the XRD evolves into three main peaks that correspond to the standard kesterite CZTS crystall structure (JCPDS card No. 26-0575). It indicate clearly the phase evolution and phase formation of CZTS with the increase of the milling time.

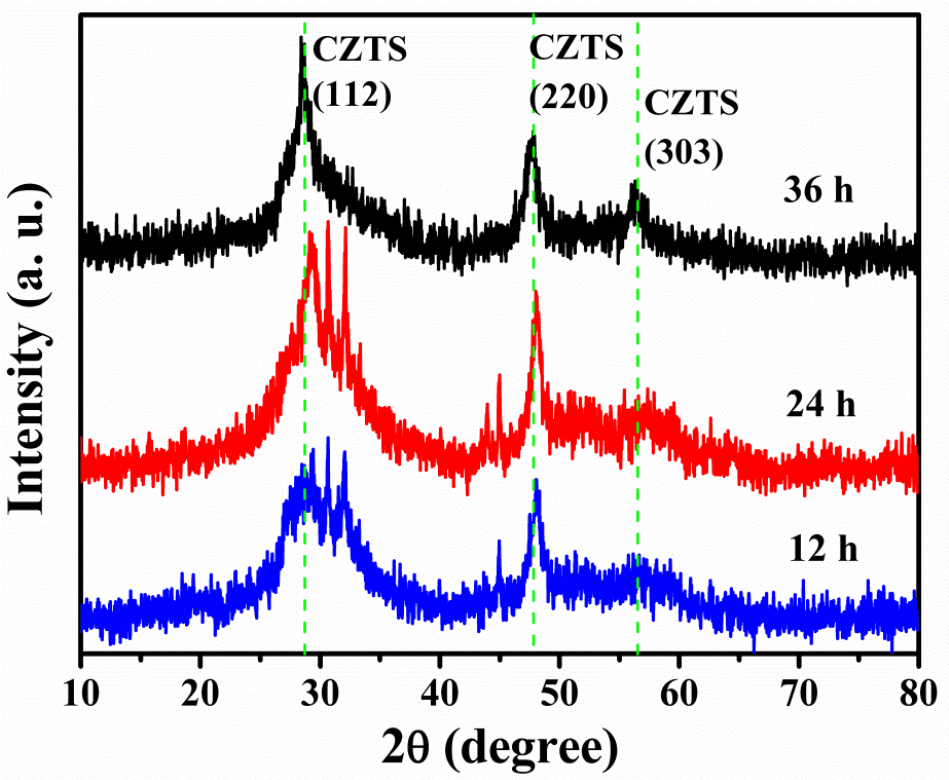

Figure S2. (a) SEM, (b) TEM, and (c) and (d) HRTEM of the CZTS precursors obtained after milling for 36 hours. (a)-(c) show the presence of a distribution of particles diameters within the narrow range of 10-20 nm with an average of 14 nm. The aggregates are composed by nanocrystallites enclosed by an armorphous phase, as shown in (c). In the nanocrystallite, the d-spacing between two crystal planes is 3.04 Å, which can be ascribed to the (112) plane of kesterite phase CZTS, as shown in (d). The ultrafine size and narrow distribution of the diameters of the synthesized CZTS NPs provide an easy suspension in a solution and are beneficial to the subsequent EPD process.

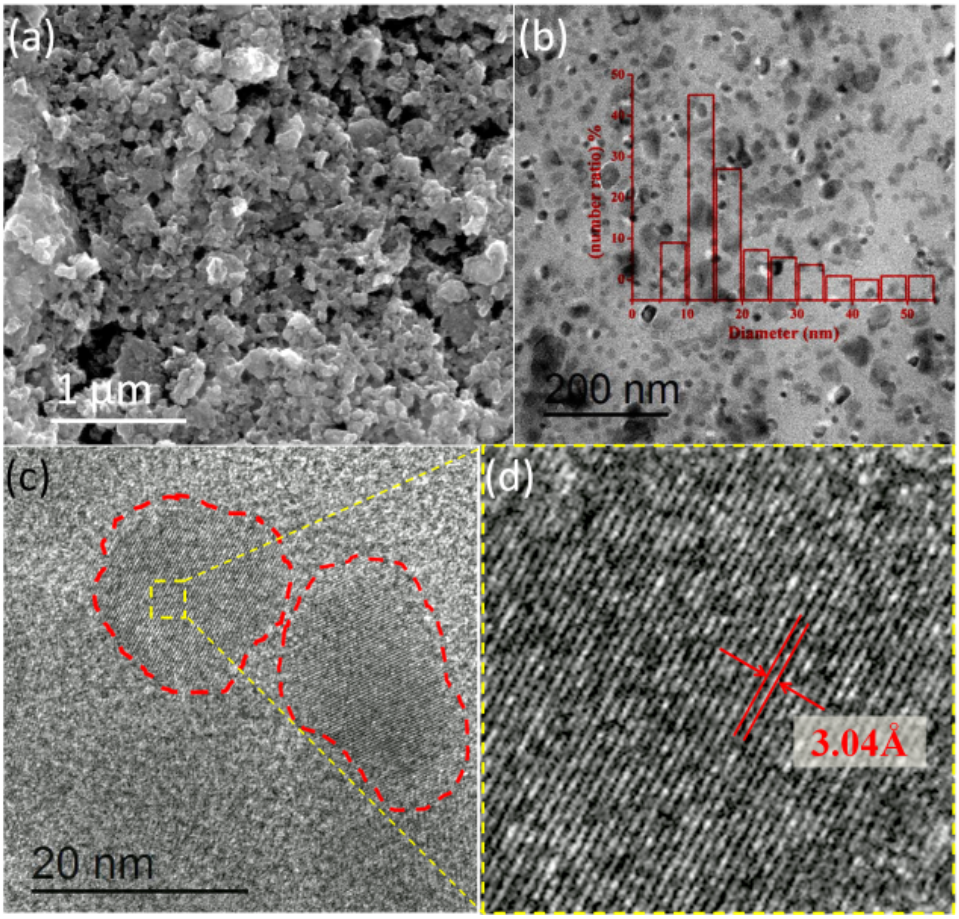

Figure S3. Morphologies of CZTS membranes obtained by annealing at (a) 450 ^{o}C, and (b) 550 ^{o}C.

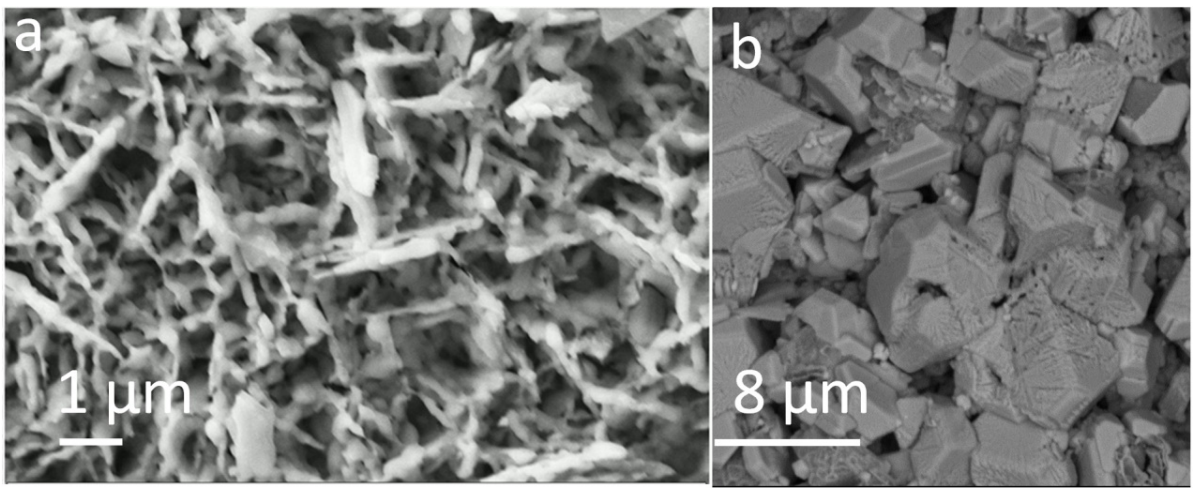

Figure S4. (a) XRD of CZTS membranes obtained by annealing at 450 ^{0}C (CZTS-450) and 500 ^{0}C (CZTS-500), respectively. As can be seen that, XRD of CZTS-500 shows a clean XRD pattern with all peaks corresponding to kesterite CZTS (JCPDS 26-0575). On the other hand, unidentified peaks are observed in the XRD of CZTS-450, indicating the presence of other sulfide impurities.

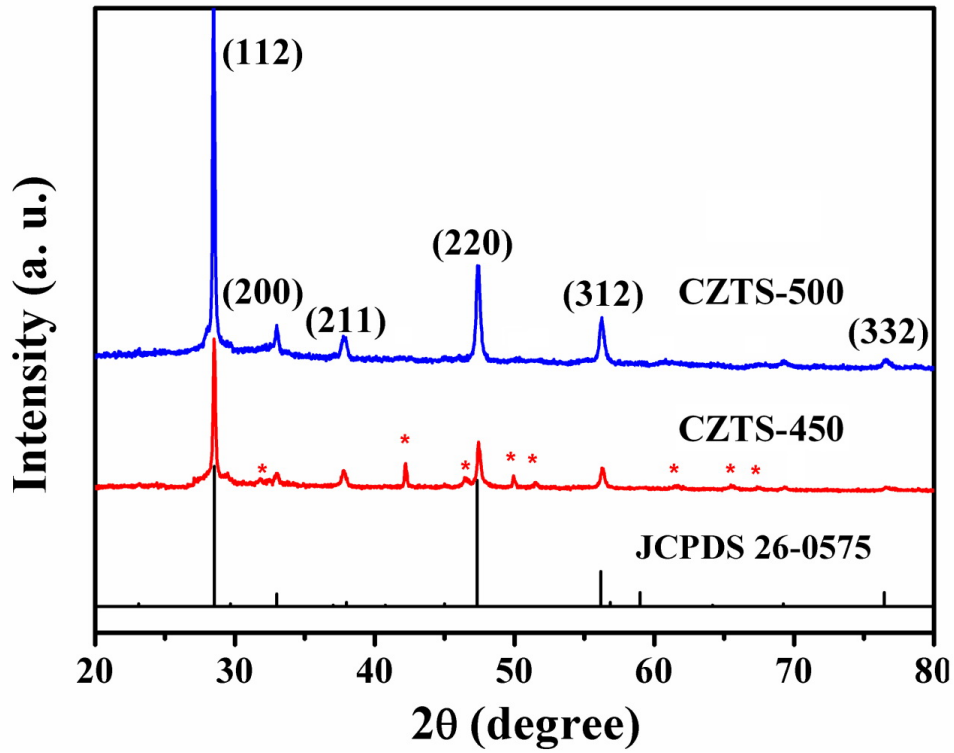

Figure S5. Deconvolution of the Raman spectra obtained from CZTS-450 and CZTS-500.

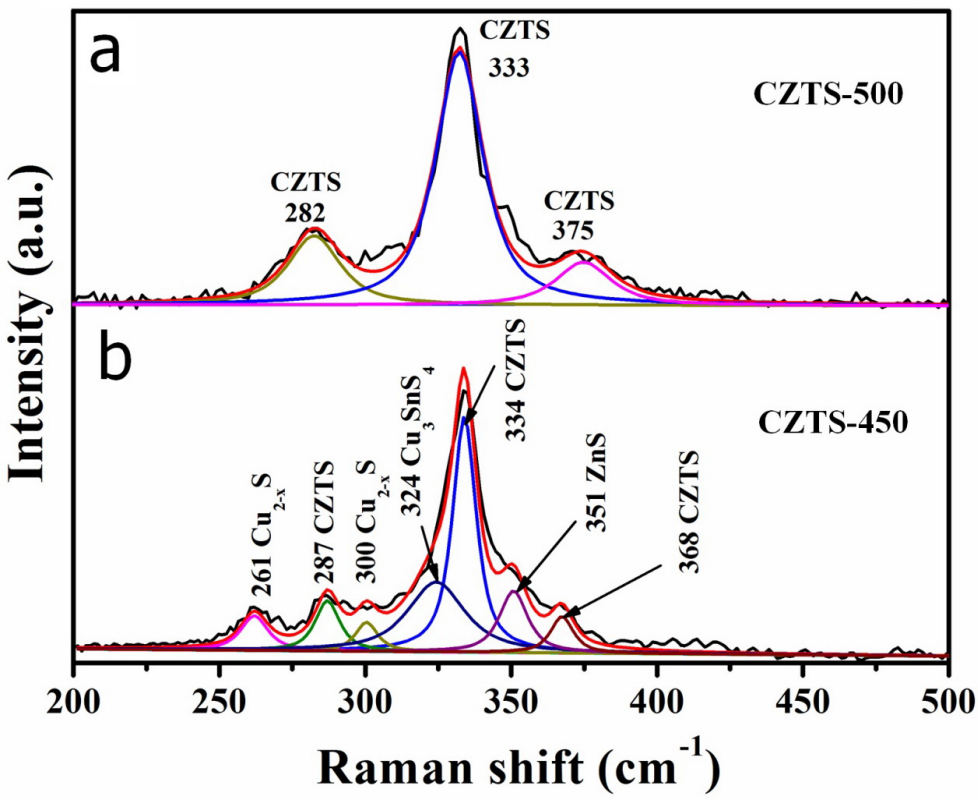

Figure S6. the infrared temperature measurement of the CZTS membranes in ambient (25 °C with ~50% of humidity) under a standard 1 Sun irradiation.

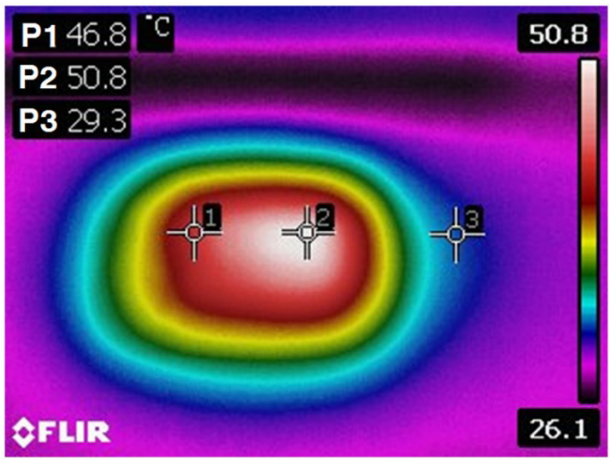

Figure S7. Temperature evolution of the water film above CZTS surface under 1 Sun irradiation. The temperature is captured in an ambient at ~25 °C with ~50% of humidity.

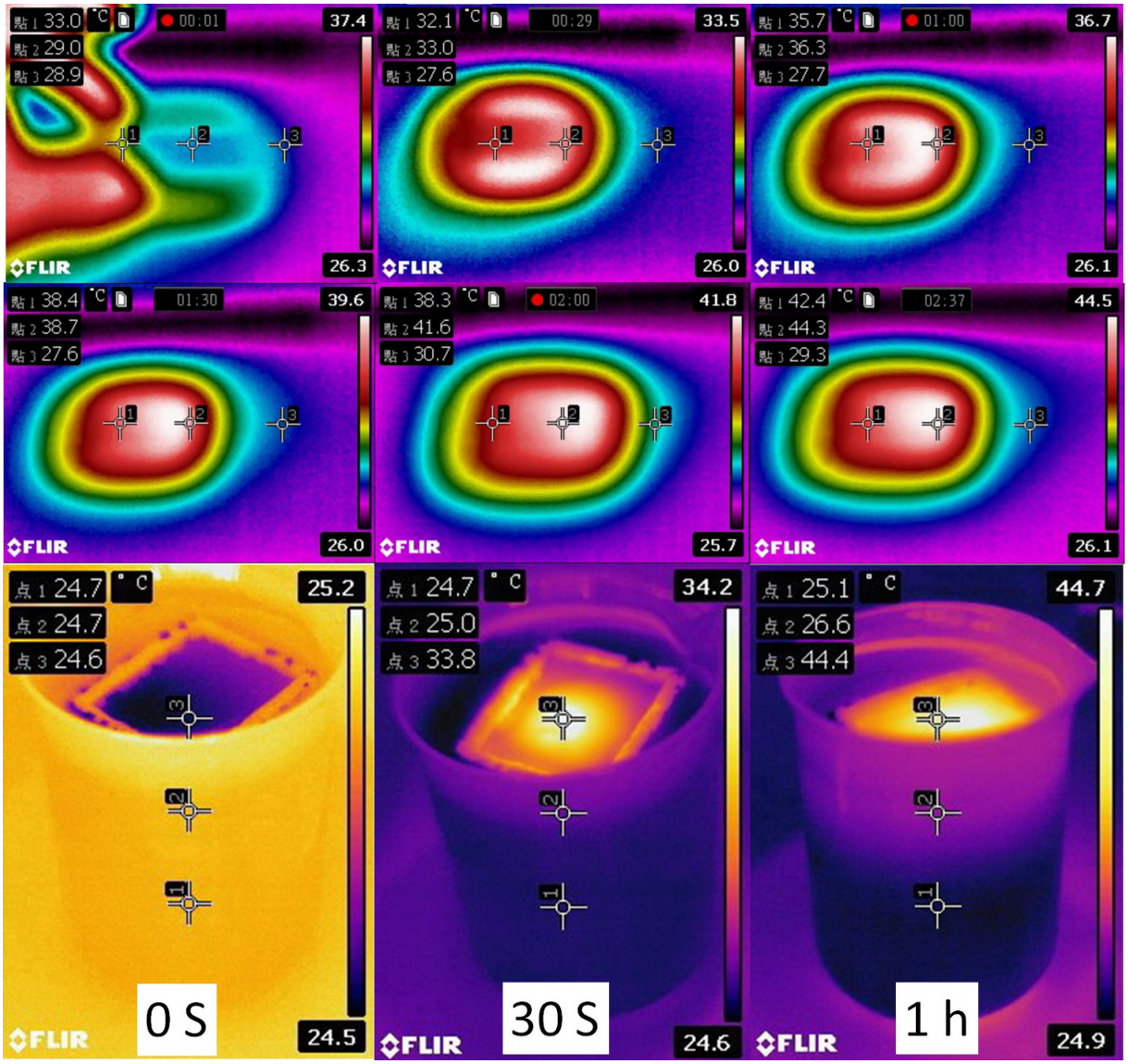

Figure S8. Schematical illustration of the set-up used for solar evaporation, in which possible heat losses are indicated.

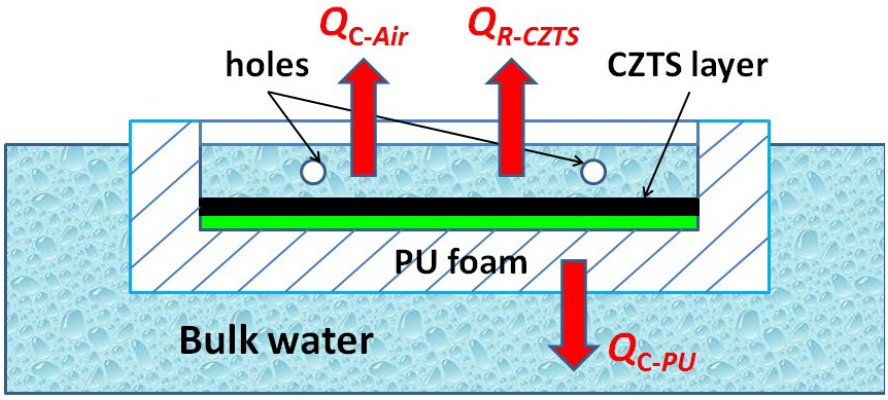

Table S1. Ingredients of the artificial sea water with 3.5% salinity.

Composition	Mass ratio in water (g/kg)
NaCl	27.5
$CaCl_2$	1.2
$MgCl_2$	5.3
K_2SO_4	1
Total mass ratio	35

Table S2. Summarization of recent solar desalination efficiency achievements.

Materials system and structure	Solar absorption efficiency	Solar Desalination Efficiency	Synthetic process	Refefences
Cu-PTFE nanocomposite films	97% in visible spectrum	------	Co-sputtering in vacuum	Appl. Phys. A[S8]
Carbon foam supported exfoliated graphite layer	97% in 250-2250 nm	85% at 10kW/m^2	Chemical routes using Nitric acid	Nat. Comm.[S9]
Au NPs on nanoporous template	99% in 400 nm-10 μm	90% at 4kW/m^2	Sputtering in vacuum	Sci. Adv.[S10]
SiO_2 core/Au shell NPs dispersed in water		80%	Colloidal chemical method	ACS Nano[S11]
polypyrrole coated stainless steel mesh		58% at 1 kW/m^2	Electropolymerization process	Adv. Mater.[S12]
Au NPs on Al_2O_3 nanorods	91% in 400-2500 nm	57% at 20 kW/m^2	Sputtering in vacuum	Nat. Comm.[S13]
Al NPs on AAO porous structure	96% in 300-2500 nm	88.4% at 4 kW/m^2, 91% at 6 kW/m^2	Vacuum evaporation	Nat. Photonics[S7]
Carbon black paper	98% in 250-2500 nm	>88% at 1 kW/m^2	Mechanical mixing	Global Challenges[S14]

3D-microporous CZTS membranes on glass	~92% in 200-2500 nm	84.5% at 1 kW/m^2, 88.8% at 5 kW/m^2	Ball milling and EPD process	**Our work**

Table S3. Ingredients of the artificial wastewater containing heavy ions.

Composition	Mass ratio in water (g/kg)	Cation concentration (g/kg)
$CdCl_2$	1.63	1
$CrCl_3$	3.045	1
$CuCl_2$	2.11	1
$PbNO_3$	1.3	1

[S1] L. Dusoulier, R. Cloots, B. Vertruyen, R. Moreno, O. Burgos-Montes, B. Ferrari, *J. Eur. Ceram. Soc.* **2011**, *31*, 1075.

[S2] M. León, S. Levcenko, R. Serna, G. Gurieva, A. Nateprov, J. M. Merino, E. J. Friedrich, U. Fillat, S. Schorr, E. Arushanov, *J. Appl. Phys.* **2010**, *108*, 093502.

[S3] F. Sun, J.-R. Ella-Menye, D. D. Galvan, T. Bai, H.-C. Hung, Y.-N. Chou, P. Zhang, S. Jiang, Q. Yu, *ACS Nano* **2015**, *9*, 2668.

[S4] a) C. G. Khoury, T. Vo-Dinh, *J. Phys. Chem. C* **2008**, *112*, 18849. b) K. Pandian Senthil, P.-S. Isabel, R.-G. Benito, F. J. G. D. Abajo, M. L.-M. Luis, *Nanotechnology* **2008**, *19*, 015606. c) E. Nalbant Esenturk, A. R. Hight Walker, *J. Raman Spectrosc.* **2009**, *40*, 86. d) S. Barbosa, A. Agrawal, L. Rodríguez-Lorenzo, I. Pastoriza-Santos, R. A. Alvarez-Puebla, A. Kornowski, H. Weller, L. M. Liz-Marzán, *Langmuir* **2010**, *26*, 14943. e) Q. Su, X. Ma, J. Dong, C. Jiang, W. Qian, *ACS Appl. Mater. Interfaces* **2011**, *3*, 1873.

[S5] C. Clavero, *Nat. Photon.* **2014**, *8*, 95.

[S6] J. M. R. Tan, Y. H. Lee, S. Pedireddy, T. Baikie, X. Y. Ling, L. H. Wong, *J. Am. Chem. Soc.* **2014**, *136*, 6684.

[S7] L. Zhou, Y. Tan, J. Wang, W. Xu, Y. Yuan, W. Cai, S. Zhu, J. Zhu, *Nat. Photon.* **2016**, *10*, 393.

[S8] M. K. Hedayati, F. Faupel, M. Elbahri, *Appl. Phys. A* **2012**, *109*, 769.

[S9] H. Ghasemi, G. Ni, A. M. Marconnet, J. Loomis, S. Yerci, N. Miljkovic, G. Chen, *Nat. Commun.* **2014**, *5*, 4449.

[S10] L. Zhou, Y. Tan, D. Ji, B. Zhu, P. Zhang, J. Xu, Q. Gan, Z. Yu, J. Zhu, *Sci. Adv.* **2016**, *2*, e1501227.

[S11] O. Neumann, A. S. Urban, J. Day, S. Lal, P. Nordlander, N. J. Halas, *ACS Nano* **2013**, *7*, 42.

[S12] L. Zhang, B. Tang, J. Wu, R. Li, P. Wang, *Adv. Mater.* **2015**, *27*, 4889.

[S13] K. Bae, G. Kang, S. K. Cho, W. Park, K. Kim, W. J. Padilla, *Nat. Commun.* **2015**, *6*, 10103.

[S14] Z. Liu, H. Song, D. Ji, C. Li, A. Cheney, Y. Liu, N. Zhang, X. Zeng, B. Chen, J. Gao, Y. Li, X. Liu, D. Aga, S. Jiang, Z. Yu, Q. Gan *Global Challenges* **2017**, *1*, 1600003.